A Direct Sampling Method Based on the Green's Function for Time-Dependent Inverse Scattering Problems

Qingqing Yu, Bo Chen*, Jiaru Wang and Yao Sun

College of Science, Civil Aviation University of China, Tianjin 300300, China.

Received 21 October 2023; Accepted (in revised version) 7 January 2024.

Abstract. This paper is devoted to numerical simulation of time domain inverse acoustic scattering problems with a point-like scatterer, multiple point-like scatterers or normal size scatterers. Using Green's functions and time convolution, we propose direct sampling methods to reconstruct the location of the scatterer. The methods involve only integral calculus without solving any equations and are easy to implement. Numerical experiments show the effectiveness and robustness of the methods.

AMS subject classifications: 65M32

Key words: Inverse scattering problem, time-dependent, direct sampling method, point-like scatterer, Green's function.

1. Introduction

The inverse scattering problems are widely used in geophysical exploration, sonar detection, non-destructive testing and medical imaging [12, 27, 31]. In the past decades, frequency domain analysis is one of the main topics in the inverse acoustic scattering studies [2, 3, 19, 23]. Nevertheless, since in practical applications the dynamic scattered data is easier to obtain, the time domain inverse scattering attracted attention of numerous researchers lately [6, 25].

This paper deals with a simple direct sampling method for inverse scattering problems in the time domain. Sampling methods play an important role in solving inverse problems. Various sampling methods, such as the linear sampling method [9, 11, 22], the direct sampling method [17], the reverse time migration method [10] and the factorization method [18], have been studied in the past decades. The basic idea of the direct sampling methods is to construct indicator functions that have different performances inside and outside the area of the scatterer. Compared to the iterative methods, sampling methods do not require a priori information of the geometry and physical properties of unknown target and can be easily implemented.

^{*}Corresponding author. Email address: charliecb@163.com (B. Chen)

For frequency domain inverse scattering problems, the linear sampling method was first proposed by Colton and Kirsch [11]. A multilevel linear sampling method and its enhancement are proposed in [21] and [20], respectively. Based on the far field operator and the far field pattern of the scattered field, a direct sampling method to reconstruct the scatterers in the frequency domain is proposed in [24]. In [5, 30], simultaneous reconstructions of an obstacle and its excitation sources in frequency domain are considered.

For time domain inverse scattering problems, the efficiency of the linear sampling method was shown by Chen *et al.* [9]. In [7, 29], the linear sampling method is used to solve the time domain inverse scattering problems in a locally perturbed half-plane and the time domain inverse scattering problems with cracks, respectively. The time domain linear sampling method is also considered to reconstruct an obstacle with Robin or Neumann boundary condition from near field measurements [16] and reconstruct penetrable obstacles [15]. Based on the migration method, effective sampling schemes to reconstruct small and extended scatterers from knowledge of time-dependent scattered data are proposed in [14].

The reconstruction of point-like scatterers has been studied by image-based direct methods in [17]. Note that the Green's function plays an important role in the analysis of the inverse problems of mathematical physics — cf. Refs. [4,6,13,26]. In [8], the approximations of the solution to the forward scattering problem are analyzed by utilizing the Green's function and the retarded single-layer potential, and an indicator function based on an approximate solution is defined to reconstruct the location of a single point-like scatterer. Unfortunately, the proposed method in [8] is not effective to reconstruct multiple point-like scatterers or normal size scatterers. In this paper, a novel direct sampling method is proposed to reconstruct point-like scatterer based on the approximate solution to the forward scattering problem and the application of the time convolution. Moreover, modified methods are defined, which are feasible to reconstruct a single point-like scatterer, multiple point-like scatterers and normal size scatterers.

The rest of the paper is organized as follows. A brief introduction of forward and inverse scattering problems under consideration is given in Section 2. In Section 3, a novel direct sampling method is proposed and the theoretical analysis of the method for reconstructing a point-like scatterer is provided. Moreover, two modified methods are also considered in this section. Numerical examples in two and three dimensional spaces presented in Section 4, show the effectiveness and robustness of the methods. Finally, the paper is concluded in Section 5.

2. Problem Setting

Let the scatterer is located in a bounded region $D \in \mathbb{R}^3$ and c > 0 be the sound speed of the homogeneous background medium in $\mathbb{R}^3 \setminus \overline{D}$. The Green's function of the D'Alembert operator $c^{-2}\partial_{tt} - \Delta$ is

$$G(x,t;y) = \frac{\delta(t - c^{-1}|x - y|)}{4\pi|x - y|}, \quad x, y \in \mathbb{R}^3, \quad x \neq y, \quad t \in \mathbb{R},$$

where Δ is the Laplacian in \mathbb{R}^3 and $\delta(t)$ is the Dirac delta distribution.

Let $\lambda(t)$ be a casual signal function. The casuality means that $\lambda(t) = 0$ for t < 0. Assume that y represents the source point such that $\{y\} \cap \overline{D} = \emptyset$. Then the incident field u^i due to y is given by

$$u^{i}(x,t;y) = G(x,t;y) * \lambda(t), \quad x \in \mathbb{R}^{3} \setminus \{y\}, \quad t \in \mathbb{R},$$

where

$$G(x,t;y) * \lambda(t) = \frac{\lambda(t - c^{-1}|x - y|)}{4\pi|x - y|}$$
(2.1)

is the time convolution of the Green's and signal functions. The time convolution (2.1) is an invaluable tool for the analysis of time domain scattering problems, which has been utilized to solve the forward scattering problem [25], reconstruct stationary point sources and a moving point source [6] and reconstruct a point-like scatterer [8].

For the analysis of the scattering problem, the total field u^{tot} is usually divided into an incident field u^i and a scattered field u, i.e. $u^{tot} = u^i + u$. The forward scattering problem for the impenetrable sound-soft obstacle *D* is to find a scattered field *u*, which satisfies the homogeneous wave equation with Dirichlet boundary condition and homogeneous initial conditions

$$c^{-2}\partial_{tt}u(x,t) - \Delta u(x,t) = 0, \quad x \in \mathbb{R}^3 \setminus \overline{D}, \quad t \in \mathbb{R},$$
 (2.2)

$$u(x,t) = -u^{i}(x,t), \qquad x \in \partial D, \qquad t \in \mathbb{R},$$
 (2.3)

$$u(x,0) = 0, x \in \mathbb{R}^3 \setminus \overline{D}, (2.4)$$

$$\partial_t u(x,0) = 0, x \in \mathbb{R}^3 \setminus \overline{D}. (2.5)$$

$$\partial_t u(x,0) = 0, \qquad x \in \mathbb{R}^3 \setminus \overline{D}.$$
 (2.5)

Note that since $\lambda(t)$ is a casual function, the incident field u^i and the scattered field u vanish for t < 0. Then the homogeneous initial conditions (2.4) and (2.5) are direct conclusions of the causality. The forward scattering problem (2.2)-(2.5) can be solved utilizing classical methods such as the retarded potential boundary integral equation method — cf. [1,25] for more details.

Assume that the region B contains D. The incident surface Γ_i and the measurement surface Γ_m where the source points and the measurement points are respectively located, are chosen as $\Gamma_i = \Gamma_m = \partial B$. Here we consider the following inverse scattering problem: Determine the location and the shape of an unknown target *D* from the partial knowledge $\{u(x,t;y):x\in\Gamma_m,t\in\mathbb{R},y\in\Gamma_i\}$ of scattered waves.

A special case of the scatterer is the point-like scatterer. For time-harmonic scattering problems with a certain wavelength, a scatterer is called point-like, if its diameter is far smaller than the wavelength. However, for time-dependent scattering problems, the wavelength is not fixed and we need the definition of the center wavelength. In the time domain, the signal function is often chosen as a Gaussian-modulated sinusoidal pulse — i.e.

$$\lambda(t) = \sin(\omega t) e^{-\sigma(t-t_0)^2},$$

where $\omega > 0$ is the center frequency, $\sigma > 0$ is the frequency bandwidth parameter and t_0 is the time-shift parameter. The center wavelength is $2\pi c/\omega$ and a scatterer is called point-like if its diameter is far smaller than the center wavelength.

3. Direct Sampling Methods

In this section, several indicator functions are defined on the basis of the analysis of the Green's function and the scattering problem with a point-like scatterer. Direct sampling methods can be established based on the indicator functions.

3.1. A direct sampling method

An approximate solution of the forward scattering problem with a point-like scatterer based on the analysis of the Green's function has been presented in [8].

Lemma 3.1 (cf. B. Chen & Y. Sun [8]). Assume that u(x,t;y) is the solution to the scattering problem (2.2)-(2.5) with a point-like scatterer D, the incident point y and the nontrivial signal function $\lambda(t)$. The incident surface Γ_i and the measurement surface Γ_m satisfy $\Gamma_i = \Gamma_m = \partial B$, where ∂B is the boundary of the region B which contains D. The diameter of the scatterer D satisfies $diam(D) = \varepsilon(x) min_{x' \in \partial D} |x - x'|$ for arbitrary $x \in \Gamma_m$, in which $0 < \varepsilon(x) \ll 1$. Denote by y_0 the geometric center of the point-like scatterer. Then we have

$$u(x,t;y) = CU_{\gamma_0}(x,t;y) + \mathcal{O}(\varepsilon'(x;y)), \quad x \in \Gamma_m, \quad t \in \mathbb{R}, \quad y \in \Gamma_i,$$

where C is a constant, which depends only on x' and D, $\varepsilon'(x;y) = \max\{\varepsilon(x), \varepsilon(y)\}$, and U_{y_0} is defined by

$$U_{y_0}(x,t;y) = -\frac{\lambda(t-c^{-1}|x-y_0|-c^{-1}|y-y_0|)}{4\pi|x-y_0||y-y_0|}.$$

Choose a sampling domain Ω such that $\Omega \cap \Gamma_m = \emptyset$ and $D \subset \Omega$. Divide the sampling region into the sampling grid with the sampling points $z \in \Omega$ as the grid points. Let u(x,t;y) be the solution to the forward scattering problem (2.2)-(2.5) with the incident point y. Using Lemma 3.1, we define the indicator function

$$I_{1}(z) = \frac{\left\| \int_{\Gamma_{m}} (u * U_{z})(x, t; y) ds_{x} \right\|_{L^{2}(\mathbb{R} \times \Gamma_{i})}^{2}}{\left\| \int_{\Gamma_{m}} (u * u)(x, t; y) ds_{x} \right\|_{L^{2}(\mathbb{R} \times \Gamma_{i})}^{2}} \int_{\Gamma_{m}} (U_{z} * U_{z})(x, t; y) ds_{x} \right\|_{L^{2}(\mathbb{R} \times \Gamma_{i})}^{2}}, \quad z \in \Omega, \quad (3.1)$$

where $(u * U_z)(x, t; y)$ denotes the time convolution of u(x, t; y) and $U_z(x, t; y)$ and

$$\|\varphi(t;y)\|_{L^2(\mathbb{R}\times\Gamma_i)} := \left(\int_{\Gamma_i}\int_{\mathbb{R}} |\varphi(t;y)|^2 dtds_y\right)^{1/2}.$$

For the reconstruction of a single point-like scatterer utilizing the indicator function $I_1(z)$, we expect that $I_1(z)$ reaches the maximum when the sampling point z coincides with the position of the point-like scatterer. For analysis, we need another indicator function — viz.

$$I_{1}^{'}(z) = \frac{\left\| \int_{\Gamma_{m}} (u * u_{z})(x, t; y) ds_{x} \right\|_{L^{2}(\mathbb{R} \times \Gamma_{i})}^{2}}{\left\| \int_{\Gamma_{m}} (u * u)(x, t; y) ds_{x} \right\|_{L^{2}(\mathbb{R} \times \Gamma_{i})} \left\| \int_{\Gamma_{m}} (u_{z} * u_{z})(x, t; y) ds_{x} \right\|_{L^{2}(\mathbb{R} \times \Gamma_{i})}}, \quad z \in \Omega, \quad (3.2)$$

where $u_z(x, t; y)$ is the solution of the scattering problem (2.2)-(2.5) when the point-like scatterer is located at $D' = \{x \in \mathbb{R}^3 \mid x - z + y_0 \in D\}$.

Theorem 3.1. Assume that u(x,t;y) is the solution to the scattering problem (2.2)-(2.5) with a point-like scatterer D, the incident point y and the nontrivial signal function $\lambda(t)$. Denote by y_0 the geometric center of D. The incident surface Γ_i and the measurement surface Γ_m satisfy $\Gamma_i = \Gamma_m = \partial B$, where ∂B is the boundary of the region B which contains D in it. The diameter of the scatterer D satisfies $\operatorname{diam}(D) = \varepsilon(x) \min_{x' \in \partial D} |x - x'|$ for arbitrary $x \in \Gamma_m$, in which $0 < \varepsilon(x) \ll 1$. Denote by Ω the sampling region that contains D in it and assume that the distance between Ω and Γ_m satisfies $\operatorname{dist}(\Omega, \Gamma_m) > \operatorname{diam}(D)$. For a point $z \in \Omega$, let $u_z(x, t; y)$ be the solution to (2.2)-(2.5) with a point-like scatterer located at $D' = \{x \in \mathbb{R}^3 | x - z + y_0 \in D\}$. The indicator function $I_1'(z)$ defined by (3.2) satisfies

$$I'_1(z) < 1, \quad z \neq y_0,$$

 $I'_1(z) = 1, \quad z = y_0.$

The indicator function $I_1(z)$ defined by (3.1) satisfies

$$I_1(z) = I_1^{'}(z) + \mathcal{O}(\varepsilon),$$

where $0 < \varepsilon \ll 1$.

Proof. Denote by $\mathscr{F}[\varphi](x,\omega;y)$ the Fourier transform of $\varphi(x,t;y)$ on the time variable t. According to the convolution theorem, the Plancherel theorem and the Cauchy-Schwarz inequality, we have

$$\begin{split} I_{1}^{'}(z) &= \frac{\left\|\mathscr{F}\left[\int_{\Gamma_{m}}\left(u * u_{z}\right) \mathrm{d}s_{x}\right]\left(\omega;y\right)\right\|_{L^{2}(\mathbb{R} \times \Gamma_{i})}^{2}}{\left\|\mathscr{F}\left[\int_{\Gamma_{m}}\left(u * u\right) \mathrm{d}s_{x}\right]\left(\omega;y\right)\right\|_{L^{2}(\mathbb{R} \times \Gamma_{i})}\left\|\mathscr{F}\left[\int_{\Gamma_{m}}\left(u_{z} * u_{z}\right) \mathrm{d}s_{x}\right]\left(\omega;y\right)\right\|_{L^{2}(\mathbb{R} \times \Gamma_{i})}} \\ &= \frac{\left\|\int_{\Gamma_{m}}\mathscr{F}\left[u\right]\left(x,\omega;y\right)\mathscr{F}\left[u_{z}\right]\left(x,\omega;y\right) \mathrm{d}s_{x}\right\|_{L^{2}(\mathbb{R} \times \Gamma_{i})}^{2}}{\left\|\int_{\Gamma_{m}}\left(\mathscr{F}\left[u\right]\left(x,\omega;y\right)\right)^{2} \mathrm{d}s_{x}\right\|_{L^{2}(\mathbb{R} \times \Gamma_{i})}\left\|\int_{\Gamma_{m}}\left(\mathscr{F}\left[u_{z}\right]\left(x,\omega;y\right)\right)^{2} \mathrm{d}s_{x}\right\|_{L^{2}(\mathbb{R} \times \Gamma_{i})}} \\ &\leq \frac{\left\|\left(\int_{\Gamma_{m}}\left(\mathscr{F}\left[u\right]\left(x,\omega;y\right)\right)^{2} \mathrm{d}s_{x}\right)^{1/2}\left(\int_{\Gamma_{m}}\left(\mathscr{F}\left[u_{z}\right]\left(x,\omega;y\right)\right)^{2} \mathrm{d}s_{x}\right)^{1/2}\right\|_{L^{2}(\mathbb{R} \times \Gamma_{i})}^{2}}{\left\|\int_{\Gamma_{m}}\left(\mathscr{F}\left[u\right]\left(x,\omega;y\right)\right)^{2} \mathrm{d}s_{x}\right\|_{L^{2}(\mathbb{R} \times \Gamma_{i})}} \leq 1. \end{split}$$

Noticing that $u_{y_0}(x, t; y) = u(x, t; y)$, we have

$$I_{1}^{'}(y_{0}) = \frac{\left\|\int_{\Gamma_{m}}(u * u_{y_{0}})(x, t; y) ds_{x}\right\|_{L^{2}(\mathbb{R} \times \Gamma_{i})}^{2}}{\left\|\int_{\Gamma_{m}}(u * u)(x, t; y) ds_{x}\right\|_{L^{2}(\mathbb{R} \times \Gamma_{i})}\left\|\int_{\Gamma_{m}}(u_{y_{0}} * u_{y_{0}})(x, t; y) ds_{x}\right\|_{L^{2}(\mathbb{R} \times \Gamma_{i})}} = 1.$$

Moreover, combining with the uniqueness of the solution to the scattering problem — cf. [9, Theorem 4], we have

$$I_{1}^{'}(z) < 1, \quad z \neq y_{0},$$

 $I_{1}^{'}(z) = 1, \quad z = y_{0}.$

Note that diam(D') = diam(D) and Lemma 3.1 imply

$$u_z(x,t;y) = CU_z(x,t;y) + \mathcal{O}(\varepsilon'(x;y)).$$

Define $\varepsilon = \sup_{x \in \Gamma_m, y \in \Gamma_i} \varepsilon'(x; y)$. Then we have $0 < \varepsilon \ll 1$ and $u_z = CU_z + \mathcal{O}(\varepsilon)$. Moreover, a direct computation yields

$$\begin{split} I_{1}^{'}(z) &= \frac{\left\| \int_{\Gamma_{m}} (u*u_{z})(x,t;y) \mathrm{d}s_{x} \right\|_{L^{2}(\mathbb{R}\times\Gamma_{i})}^{2}}{\left\| \int_{\Gamma_{m}} (u*u)(x,t;y) \mathrm{d}s_{x} \right\|_{L^{2}(\mathbb{R}\times\Gamma_{i})}^{2} \left\| \int_{\Gamma_{m}} (u_{z}*u_{z})(x,t;y) \mathrm{d}s_{x} \right\|_{L^{2}(\mathbb{R}\times\Gamma_{i})}^{2}} \\ &= \frac{\left\| \int_{\Gamma_{m}} (u*(CU_{z} + \mathcal{O}(\varepsilon)))(x,t;y) \mathrm{d}s_{x} \right\|_{L^{2}(\mathbb{R}\times\Gamma_{i})}^{2}}{\left\| \int_{\Gamma_{m}} (u*u)(x,t;y) \mathrm{d}s_{x} \right\|_{L^{2}(\mathbb{R}\times\Gamma_{i})}^{2}} \\ &\times \frac{1}{\left\| \int_{\Gamma_{m}} ((CU_{z} + \mathcal{O}(\varepsilon))*(CU_{z} + \mathcal{O}(\varepsilon)))(x,t;y) \mathrm{d}s_{x} \right\|_{L^{2}(\mathbb{R}\times\Gamma_{i})}^{2}} \\ &= \frac{C^{2} \left\| \int_{\Gamma_{m}} (u*U_{z})(x,t;y) \mathrm{d}s_{x} \right\|_{L^{2}(\mathbb{R}\times\Gamma_{i})}^{2} + \mathcal{O}(\varepsilon)}{\left\| \int_{\Gamma_{m}} (u*u)(x,t;y) \mathrm{d}s_{x} \right\|_{L^{2}(\mathbb{R}\times\Gamma_{i})}^{2} \left(C^{2} \left\| \int_{\Gamma_{m}} (U_{z}*U_{z})(x,t;y) \mathrm{d}s_{x} \right\|_{L^{2}(\mathbb{R}\times\Gamma_{i})}^{2} + \mathcal{O}(\varepsilon) \right)} \\ &= \frac{\left\| \int_{\Gamma_{m}} (u*u)(x,t;y) \mathrm{d}s_{x} \right\|_{L^{2}(\mathbb{R}\times\Gamma_{i})}^{2} \left(\left\| \int_{\Gamma_{m}} (U_{z}*U_{z})(x,t;y) \mathrm{d}s_{x} \right\|_{L^{2}(\mathbb{R}\times\Gamma_{i})}^{2} + \mathcal{O}(\varepsilon)} \\ &= I_{1}(z) + \mathcal{O}(\varepsilon). \end{split}$$

This completes the proof.

According to Theorem 3.1, we can derive that the indicator function $I_1(z)$ reaches its global maximum if and only if $z = y_0$, and $I_1(z)$ is an approximation of $I_1(z)$. Then we can say that, approximately, $I_1(z)$ reaches its global maximum if and only if $z = y_0$. Thus, we can get the approximate location of the point-like scatterer by drawing the image of $I_1(z)$. The algorithm can be summarized as Algorithm 3.1. The feasibility of the algorithm to reconstruct a point-like scatterer is verified by the numerical experiments in the next section.

Algorithm 3.1 The Reconstruction Scheme Using the Indicator Function $I_1(z)$.

Step 1. Choose the scatterer D, the signal function $\lambda(t)$, the incident surface Γ_i and the measurement surface $\Gamma_m = \Gamma_i$. Select the sensing points $x_i \in \Gamma_m$, $i = 1, ..., N_m$, the equidistant time nodes $t_k \in [0, T]$, $k = 0, ..., N_t$ and the source points $y_j \in \Gamma_i$, $j = 1, ..., N_i$. Collect the scattered data on Γ_m : $u(x_i, t_k; y_j)$, $i = 1, ..., N_m$, $k = 0, ..., N_t$, $j = 1, ..., N_i$.

Step 2. Choose a cubic sampling domain Ω such that $D \subset \Omega$, $\overline{\Omega} \cap \Gamma_m = \emptyset$. Divide Ω into equidistant sampling grid, for any sampling point $z \in \Omega$, compute

$$\begin{split} N_{u,U_{z}}(z) &= \left(\sum_{j=1}^{N_{i}}\sum_{k=0}^{N_{t}}\left|\sum_{i=1}^{N_{m}}\sum_{l=0}^{k}u(x_{i},t_{k-l};y_{j})U_{z}(x_{i},t_{l};y_{j})\Delta t\Delta s_{x_{i}}\right|^{2}\Delta t\Delta s_{y_{j}}\right)^{1/2},\\ N_{u,u}(z) &= \left(\sum_{j=1}^{N_{i}}\sum_{k=0}^{N_{t}}\left|\sum_{i=1}^{N_{m}}\sum_{l=0}^{k}u(x_{i},t_{k-l};y_{j})u(x_{i},t_{l};y_{j})\Delta t\Delta s_{x_{i}}\right|^{2}\Delta t\Delta s_{y_{j}}\right)^{1/2},\\ N_{U_{z},U_{z}}(z) &= \left(\sum_{j=1}^{N_{i}}\sum_{k=0}^{N_{t}}\left|\sum_{i=1}^{N_{m}}\sum_{l=0}^{k}U_{z}(x_{i},t_{k-l};y_{j})U_{z}(x_{i},t_{l};y_{j})\Delta t\Delta s_{x_{i}}\right|^{2}\Delta t\Delta s_{y_{j}}\right)^{1/2}, \end{split}$$

and

$$I_1(z) = \frac{N_{u,U_z}^2(z)}{N_{u,u}(z)N_{U_z,U_z}(z)},$$

where Δt is the length of the time step, Δs_{x_i} and Δs_{y_j} are the areas of the grid cells of the sensor x_i and the source y_j , respectively.

Step 3. Mesh $I_1(z)$ on the sampling grid. The location of the point-like scatterer is determined by the global maximum point of $I_1(z)$.

Remark 3.1. A time shift parameter μ appears in the numerical computation of the time domain inverse scattering problems — cf. [7,8,15]. The time shift parameter has a significant impact on the reconstruction of the scatterer. However, the theoretical analysis of the time shift is scarce and the time-shift parameter is usually chosen by trial and error in the numerical experiments.

In the definition of the indicator function (3.1), we choose the time convolution of u and U_z instead of the product noted in [8]. An important property of the convolution is

$$(\tau_{\mu}f) * g = f * (\tau_{\mu}g) = \tau_{\mu}(f * g),$$

where τ_{μ} is the time shift operator defined by $(\tau_{\mu}f)(t) = f(t-\mu)$. On this basis, we have

$$\int_{\mathbb{R}} \left| \left((\tau_{\mu} f) * g \right) (t) \right|^2 dt = \int_{\mathbb{R}} \left| \left(\tau_{\mu} (f * g) \right) (t) \right|^2 dt = \int_{\mathbb{R}} \left| (f * g) (t) \right|^2 dt.$$

The property is found interesting since the time shift is no longer an important factor when we utilize the time convolution in the indicator function.

3.2. Modified indicator functions

For $x \in \Gamma_m$, $t \in \mathbb{R}$ and $z \in \Omega$, compare the functions

$$U_z(x,t;y) = -\frac{\lambda(t-c^{-1}|x-z|-c^{-1}|y-z|)}{4\pi|x-z||y-z|}$$

and

$$(G*\lambda)(x,t;z) = \frac{\lambda(t-c^{-1}|x-z|)}{4\pi|x-z|}.$$

Note that the difference between the signal functions $\lambda(t-c^{-1}|x-z|-c^{-1}|y-z|)$ and $\lambda(t-c^{-1}|x-z|)$ is the time shift $c^{-1}|y-z|$. Define

$$\begin{split} f_{1,z}(x,t;y) &:= u(x,t;y) * \lambda(t-c^{-1}|x-z|), \\ f_{2,z}(x,t;y) &:= u(x,t;y) * \lambda(t-c^{-1}|x-z|-c^{-1}|y-z|). \end{split}$$

According to Remark 3.1, we have

$$f_{2,z}(x,t;y) = f_{1,z}(x,t-c^{-1}|y-z|;y),$$

and direct computations give

$$\begin{split} & \left\| \int_{\Gamma_m} f_{2,z}(x,t;y) \mathrm{d}s_x \right\|_{L^2(\mathbb{R} \times \Gamma_i)} \\ &= \left\| \int_{\Gamma_m} f_{1,z}(x,t-c^{-1}|y-z|;y) \mathrm{d}s_x \right\|_{L^2(\mathbb{R} \times \Gamma_i)} \\ &= \left\| \int_{\Gamma_m} f_{1,z}(x,t;y) \mathrm{d}s_x \right\|_{L^2(\mathbb{R} \times \Gamma_i)}, \end{split}$$

which means that $U_z(x,t;y)$ and $(G*\lambda)(x,t;z)$ play similar roles while calculating time convolutions.

Using the notation

$$G_z(x,t) = (G * \lambda)(x,t;z),$$

we define a new indicator function — viz.

$$I_2(z) = \frac{\left\| \int_{\Gamma_m} (u * G_z)(x,t;y) \mathrm{d}s_x \right\|_{L^2(\mathbb{R} \times \Gamma_t)}^2}{\left\| \int_{\Gamma_m} (u * u)(x,t;y) \mathrm{d}s_x \right\|_{L^2(\mathbb{R} \times \Gamma_t)} \left\| \int_{\Gamma_m} (U_z * U_z)(x,t;y) \mathrm{d}s_x \right\|_{L^2(\mathbb{R} \times \Gamma_t)}}, \quad z \in \Omega.$$

Note that only the molecular is slightly modified in $I_2(z)$ compared to $I_1(z)$. Therefore, a new algorithm based on the indicator function $I_2(z)$ is similar to Algorithm 3.1 except that we use

$$I_2(z) = \frac{N_{u,G_z}^2(z)}{N_{u,u}(z)N_{U_z,U_z}(z)}$$

instead of $I_1(z)$ as the indicator, in which $N_{u,u}(z)$ and $N_{U_z,U_z}(z)$ are defined the same as that in Algorithm 3.1 and

$$N_{u,G_z}(z) = \left(\sum_{i=1}^{N_i} \sum_{k=0}^{N_t} \left| \sum_{i=1}^{N_m} \sum_{l=0}^{k} u(x_i, t_{k-l}; y_j) G_z(x_i, t_l) \Delta t \Delta s_{x_i} \right|^2 \Delta t \Delta s_{y_j} \right)^{1/2}.$$

Furthermore, notice that $\|\int_{\Gamma_m} (u*u)(x,t;y) \mathrm{d} s_x\|_{L^2(\mathbb{R}\times\Gamma_i)}$ is independent of z and has no influence to the effect of the algorithm. Based on this thought, we go a step further and define a new modified indicator function

$$I_3(z) = \left\| \int_{\Gamma_m} (u * G_z)(x, t; y) ds_x \right\|_{L^2(\mathbb{R} \times \Gamma_i)}, \quad z \in \Omega.$$

Once again, a new algorithm based on the indicator function $I_3(z)$ is similar to Algorithm 3.1, except that

$$I_3(z) = N_{u,G_a}(z)$$

is used as the indicator.

Note that algorithm based on the indicator function $I_3(z)$ is feasible to reconstruct a single point-like scatterer, multiple point-like scatterers, a normal size scatterer or some of the more complicated cases. The effectiveness and robustness of the algorithm can be seen in Section 4.

4. Numerical Experiments

This section demonstrates the effectiveness of the proposed algorithms with numerical experiments in both two and three dimensional spaces. In \mathbb{R}^2 , the Green's function of the D'Alembert operator $c^{-2}\partial_{tt} - \Delta$ is

$$G_2(x,t;y) = \frac{H(t-c^{-1}|x-y|)}{2\pi\sqrt{t^2-c^{-2}|x-y|^2}}, \quad x,y \in \mathbb{R}^2, \quad x \neq y, \quad t \in \mathbb{R},$$

where H(t) is the Heaviside function

$$H(t) = 1, \quad t > 0,$$

$$H(t) = 0, \quad t \le 0.$$

The time convolution of the Green's function and the signal function is

$$G_{2}(x,t;y) * \lambda(t)$$

$$= \int_{-\infty}^{t-c^{-1}|x-y|} \frac{\lambda(\tau)}{2\pi\sqrt{(t-\tau)^{2}-c^{-2}|x-y|^{2}}} d\tau, \quad x,y \in \mathbb{R}^{2}, \quad x \neq y, \quad t \in \mathbb{R}.$$

In the experiments, $N=N_i=N_m$ denote the number of the incident/measurement points. The time interval [0,T] is equally divided into N_t time steps. Choose the sound speed in the homogeneous background medium as c=1. The random noise is added to the scattered data by

$$u_{\varepsilon} = u(1 + \varepsilon r),$$

where ε denotes the noise level and r are uniformly distributed random numbers ranging from -1 to 1. The signal function is chosen to be a sinusoidal pulse

$$\lambda(t) = \sin(4t)e^{-1.6(t-3)^2}$$
.

Unless otherwise specified, in the experiments in \mathbb{R}^2 , we choose T=25 for Algorithms 3.1 and the algorithm based on the indicator function $I_2(z)$, T=15 for algorithm based on the indicator function $I_3(z)$, and $N_t=128$ for all the three algorithms. N=20 is chosen for the reconstructions with full aperture data. The measurement points are evenly distributed on the circle of radius 4 with the center at the origin, which means the measurement points are

$$x_i = 4\left(\cos\frac{i\pi}{10}, \sin\frac{i\pi}{10}\right), \quad i = 0, 1, \dots, 19.$$

As sampling points we chose 21×21 uniformly distributed points in the sampling region $\Omega = [-2.6, 2.6] \times [-2.6, 2.6]$.

Example 4.1 (Reconstructions of a point-like scatterer). In this example, we reconstruct a point-like scatterer utilizing the Algorithms 3.1 and the algorithms based on the indicator functions $I_2(z)$ and $I_3(z)$. The boundary of the scatterer is parameterized as

$$s(\theta) = (a, b) + 0.001(\cos \theta, \sin \theta), \quad \theta \in [0, 2\pi).$$
 (4.1)

The reconstructions of point-like scatterers centered at (a, b) = (0, 0) with different noise are shown in Fig. 1. The measurement points are marked with black asterisks and the green asterisks represent the exact locations of the point-like scatterers. Fig. 1 shows that the algorithms are feasible and robust to reconstruct a point-like scatterer.

Example 4.2 (Reconstructions of multiple point-like scatterers). The simultaneous reconstructions of multiple point-like scatterers are considered in this example. The boundaries of the scatterers are also parameterized as (4.1) with different centers (a, b). Fig. 2 shows the reconstructions of different numbers of point-like scatterers with the noise level $\varepsilon = 5\%$. The exact locations of the scatterers are marked with green asterisks.

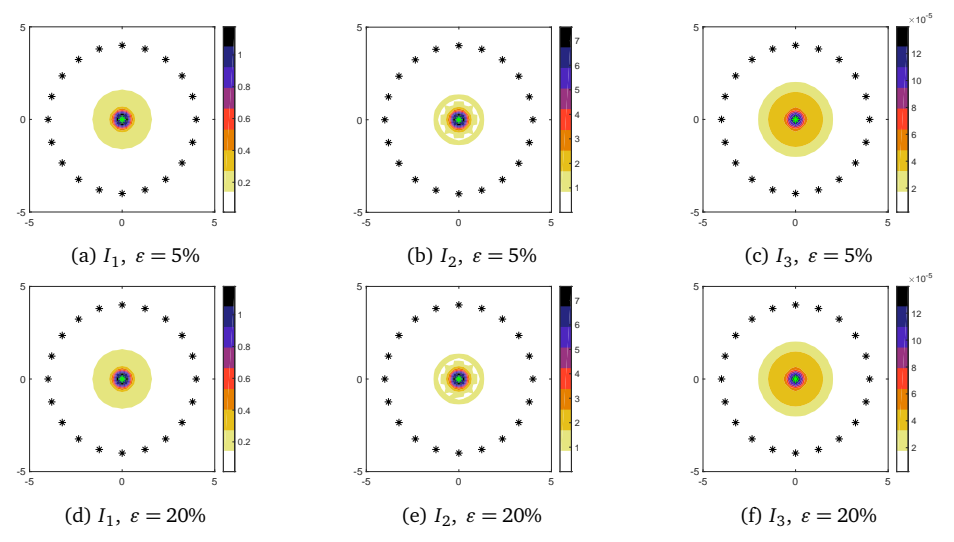


Figure 1: Reconstructions of a single point-like scatterer centered at (0,0) with different indicators and noise levels.

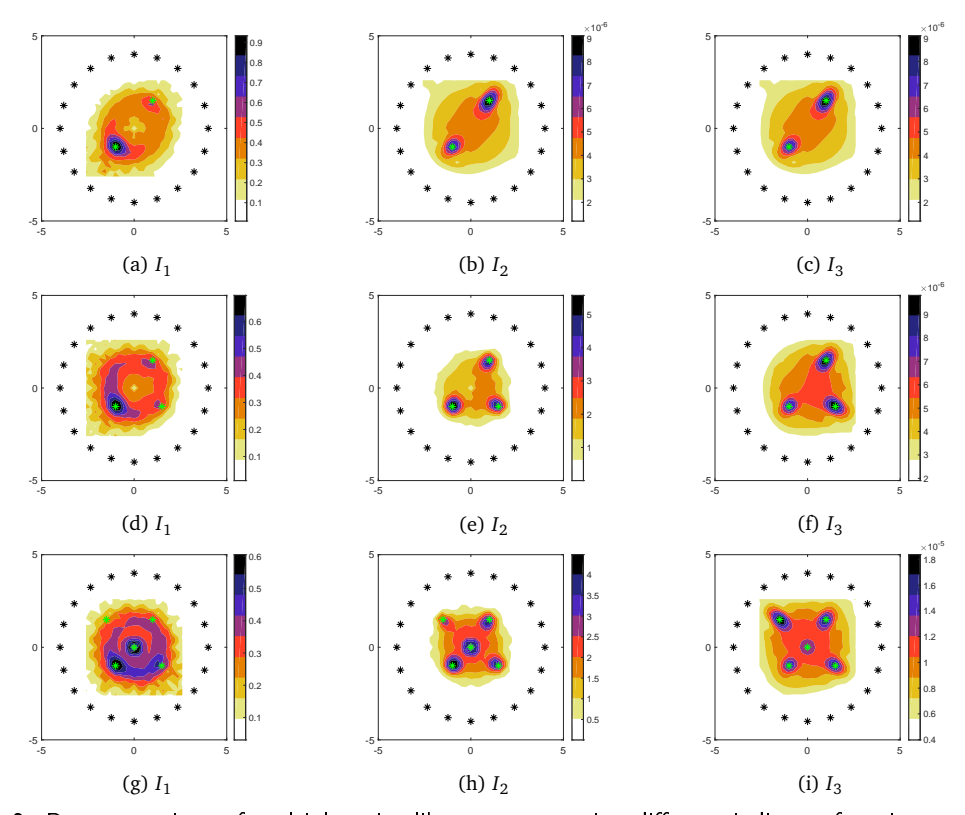


Figure 2: Reconstructions of multiple point-like scatterers using different indicator functions, $\varepsilon=5\%$. (a)-(c) Reconstructions of 2 point-like scatterers centered at (-1,-1) and (1,1.5), respectively. (d)-(f) Reconstructions of 3 point-like scatterers centered at (-1,-1), (1,1.5) and (1.5,-1), respectively. (g)-(i) Reconstructions of 5 point-like scatterers centered at (-1,-1), (1,1.5), (1.5,-1), (-1.5,1.5) and (0,0), respectively.

Example 4.3 (Reconstructions of a normal size scatterer). Consider the reconstructions of a normal size scatterer from both full and limited aperture scattered data. The boundaries of the scatterers, such as the circle-shaped scatterer, the kite-shaped scatterer and the starfish-shaped scatterer, can be parameterized as

Circle : $s(\theta) = (a, b) + 1.5(\cos \theta, \sin \theta)$, $\theta \in [0, 2\pi)$, (4.2) Kite : $s(\theta) = (a, b) + (\cos \theta + 0.65\cos 2\theta - 0.65, 1.5\sin \theta)$, $\theta \in [0, 2\pi)$, (4.3) Starfish : $s(\theta) = (a, b) + (1 + 0.2\cos 5\theta)(\cos \theta, \sin \theta)$, $\theta \in [0, 2\pi)$. (4.4)

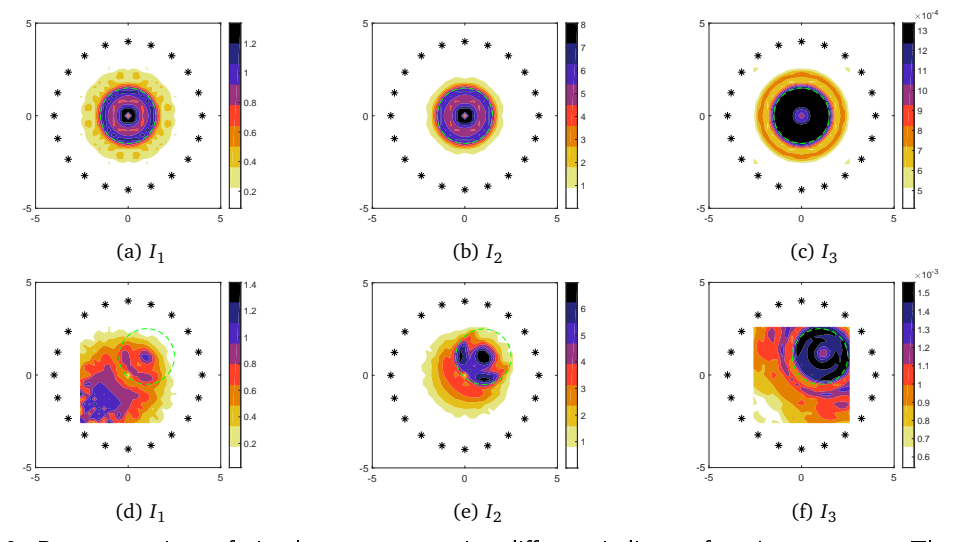


Figure 3: Reconstructions of circular scatterers using different indicator functions, $\varepsilon = 5\%$. The circles are centered at (0,0) in the first row and centered at (1,1) in the second row.

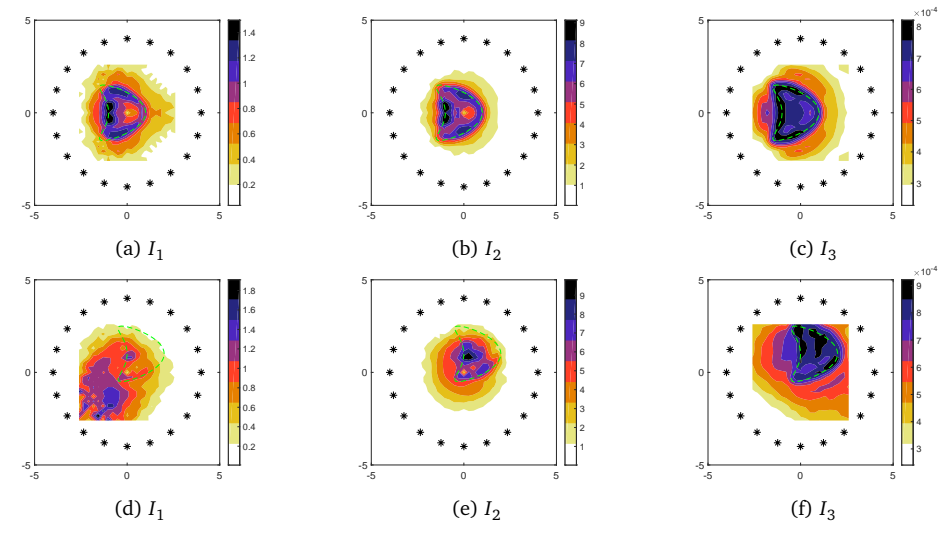


Figure 4: Reconstructions of kite-shaped scatterers using different indicator functions, $\varepsilon = 5\%$. The kite is centered at (0,0) in the first row and centered at (1,1) in the second row.

The reconstructions of the three kinds of scatterers with full aperture data and the reconstructions of the starfish-shaped scatterer using limited aperture data are provided in Figs. 3-6. For the reconstructions from limited aperture data, N=10 and N=15 are chosen for the apertures $\theta=\pi$ and $\theta=(3/2)\pi$, respectively. The coordinates of the measurement points are

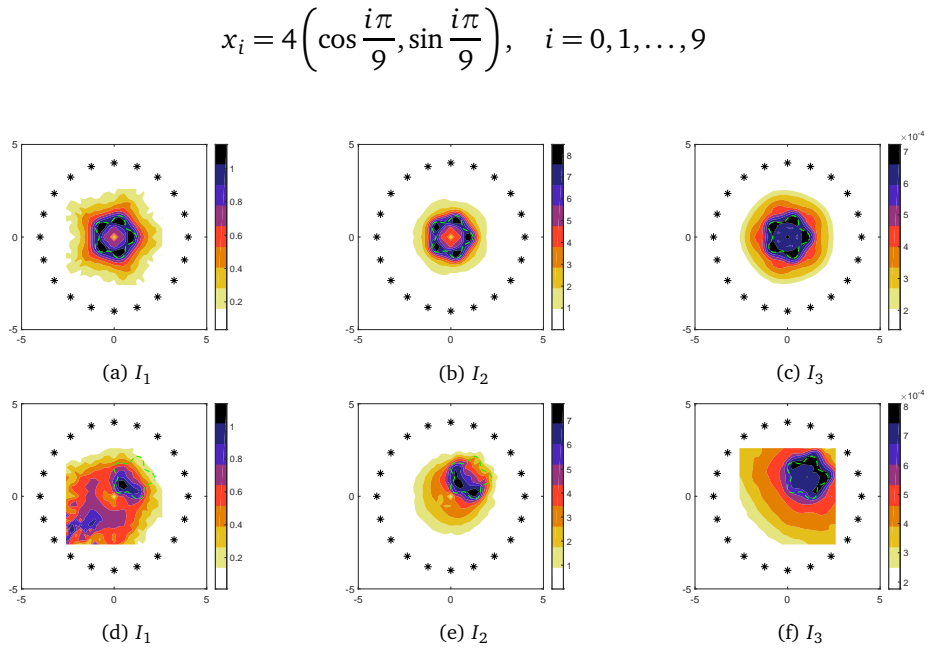


Figure 5: Reconstructions of starfish-shaped scatterers using different indicator functions, $\varepsilon = 5\%$. The starfish is centered at (0,0) in the first row and centered at (1,1) in the second row.

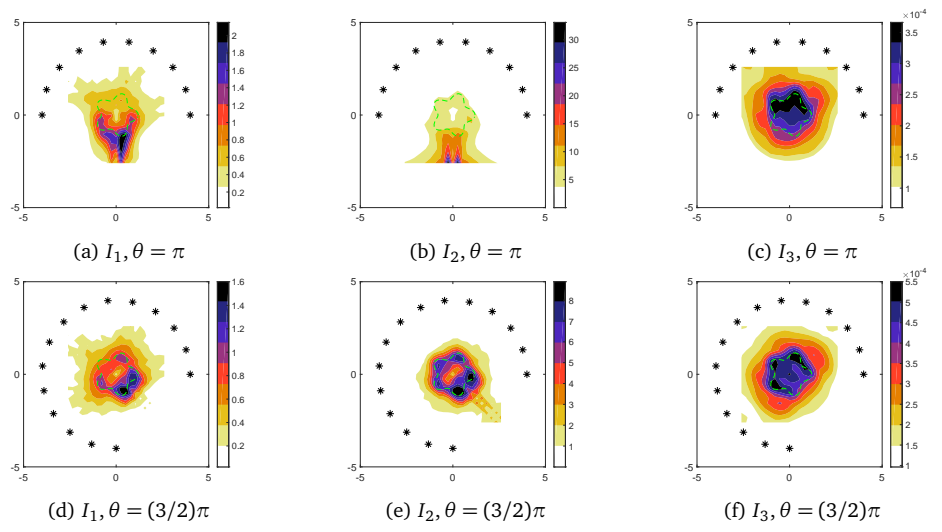


Figure 6: Reconstructions of starfish-shaped scatterer centered at (0,0) from limited aperture data using different indicator functions, $\varepsilon = 5\%$.

for the aperture $\theta = \pi$ and

$$x_i = 4\left(\cos\frac{3i\pi}{28}, \sin\frac{3i\pi}{28}\right), \quad i = 0, 1, \dots, 14$$

for the aperture $\theta = (3/2)\pi$. The exact boundaries of the scatterers are marked with green dash lines. From Figs. 3-6, we can find that Algorithms 3.1 and the algorithm based on the indicator function $I_2(z)$ can roughly reconstruct a normal size scatterer centered at (a,b)=(0,0), but are not feasible to reconstruct a scatterer that is not centered at the origin. Nevertheless, the algorithm based on the indicator function $I_3(z)$ can reconstruct a normal size scatterer no matter the scatterer is centered at the origin or not. For the reconstructions of the scatterers with limited aperture data, only the part of the boundary curve that is close to the measurement points can be well reconstructed.

Example 4.4 (Simultaneous reconstructions of a normal size scatterer and a point-like scatterer). Simultaneous reconstructions of a normal size scatterer and a point-like scatterer are now considered. The boundaries of the point-like, acorn-shaped and rounded-square-shaped scatterers centered at (a, b) are respectively parameterized as

$$s(\theta) = (a, b) + 0.1(\cos \theta, \sin \theta), \qquad \theta \in [0, 2\pi), \tag{4.5a}$$

$$s(\theta) = (a, b) + 0.84 \left(\frac{17}{4} + 2\cos 3\theta\right)^{1/2} (\cos \theta, \sin \theta), \qquad \theta \in [0, 2\pi), \tag{4.5b}$$

$$s(\theta) = (a, b) + \frac{\sqrt{2}}{2} \left(\cos^3 \theta + \sin^3 \theta + \cos \theta + \sin \theta, -\cos^3 \theta + \sin^3 \theta - \cos \theta + \sin \theta\right), \quad \theta \in [0, 2\pi).$$

$$(4.5c)$$

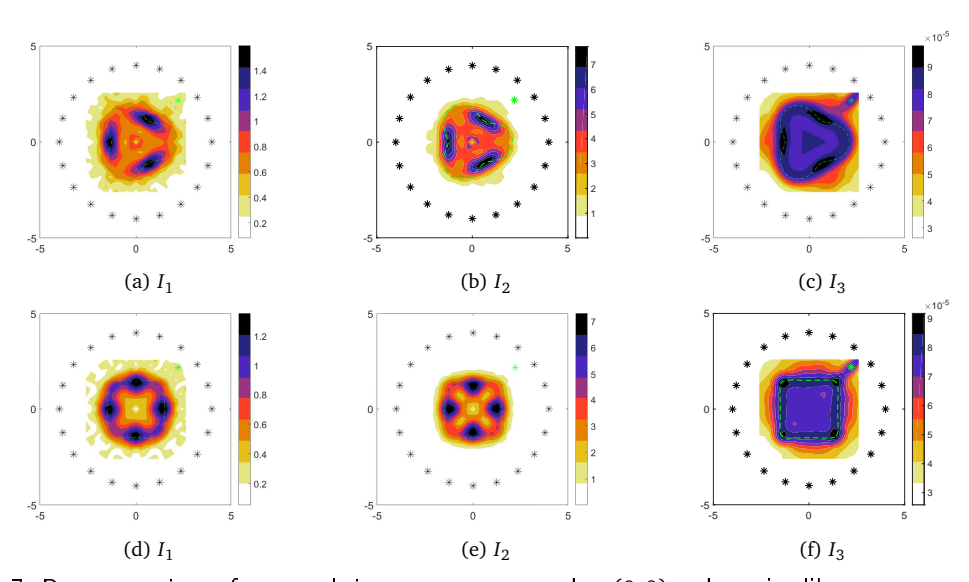


Figure 7: Reconstructions of a normal size scatterer centered at (0,0) and a point-like scatterer centered at (2.2,2.2) using different indicator functions, $\varepsilon=5\%$. (a)-(c) Reconstructions of the acorn-shaped scatterer and the point-like scatterer. (d)-(f) Reconstructions of the rounded-square-shaped scatterer and the point-like scatterer.

The point-like scatterer is chosen to be centered at (2.2, 2.2), which is marked with green asterisk. The acorn-shaped and rounded-square-shaped scatterers are centered at (0,0), the exact boundaries are marked with green dash lines. The reconstructions are shown in Fig. 7. The result shows that the algorithm based on the indicator function $I_3(z)$ can roughly reconstruct the shapes of acorn-shaped or rounded-square-shaped scatterers together with the location of the point-like scatterer.

Example 4.5 (Reconstructions of two disconnected normal size scatterers). Consider the reconstructions of two disconnected normal size scatterers using the algorithm based on the indicator function $I_3(z)$. The boundaries of the circle-shaped, kite-shaped, acorn-shaped and starfish-shaped scatterers are parameterized similar as (4.2)-(4.5) except that the sizes of the scatterers are chosen to be respectively four-ninths, half, half and two-thirds of the original sizes. The boundary of the peanut-shaped scatterer centered at (a, b) is parameterized as

$$s(\theta) = (a, b) + \frac{5}{12} (4\cos^2\theta + \sin^2\theta)^{1/2} (\cos\theta, \sin\theta), \quad \theta \in [0, 2\pi).$$

Choose the noise level $\varepsilon = 5\%$, the terminal time T = 25 and $N_t = 256$. The reconstructions are shown in Fig. 8. The exact boundaries of the scatterers are marked with green dash lines, the measurement points are marked with black asterisks.

In the following two examples, we consider the effectiveness of the algorithm based on the indicator function $I_3(z)$ to reconstruct point-like scatterers and cubes in \mathbb{R}^3 . Note that the computation cost of the three-dimensional time domain forward scattering problem is expensive and the k-Wave software is utilized for the calculation [28]. In Examples 4.6-4.7, the measurement surface Γ_m is chosen to be a spherical surface centered at the origin with radius 4, the incident surface is chosen as $\Gamma_i = \Gamma_m$. Denote by N the number of the measurement points and incident points whose locations are generated by the function makeCartSphere utilizing the k-Wave software. The Cartesian coordinates of the measurement points for $i=0,1,\ldots,N-1$ are

$$x_{i} = 4\left(\sqrt{1 - \alpha_{i}^{2}}\cos(3 - \sqrt{5})i\pi, \alpha_{i}, \sqrt{1 - \alpha_{i}^{2}}\sin(3 - \sqrt{5})i\pi\right), \quad \alpha_{i} = \frac{2i - N + 1}{N}.$$

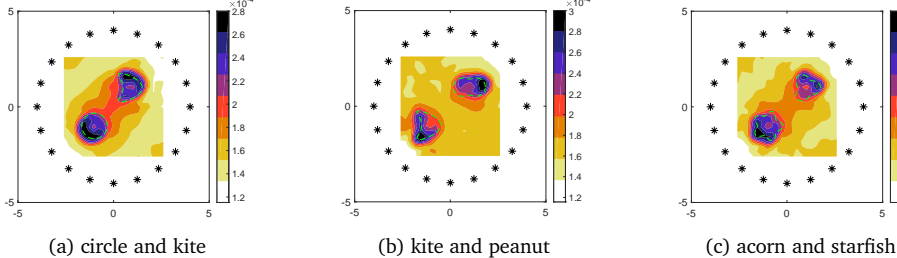


Figure 8: Reconstructions of two disconnected normal size scatterers using the indicator function I_3 , $\varepsilon=5\%$. (a) The circle-shaped scatterer centered at (-1,-1) and the kite-shaped scatterer centered at (1,1). (b) The kite-shaped scatterer centered at (-1,-1) and peanut-shaped scatterer centered at (1,1). (c) The acorn-shaped scatterer centered at (-1,-1) and the starfish-shaped scatterer centered at (1,1).

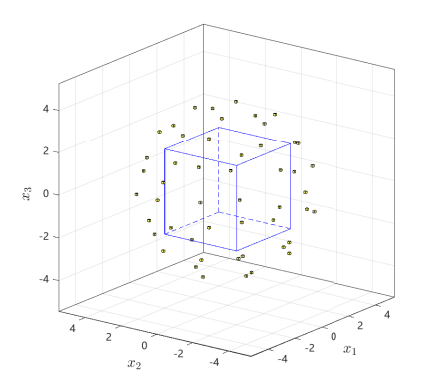


Figure 9: The geometric diagram of the measurement points and sampling region.

The sampling points are chosen as $21 \times 21 \times 21$ equidistant points in the sampling region $\Omega = [-2, 2] \times [-2, 2] \times [-2, 2]$. The geometric diagram of the measurement points and sampling region is shown in Fig. 9. The noise level is chosen as $\varepsilon = 5\%$.

Example 4.6 (Reconstructions of point-like scatterers in \mathbb{R}^3). Consider the reconstructions of point-like scatterers by choosing N=50, T=19 and $N_t=256$. The exact locations of the point-like scatterers are marked with green asterisks. In fact, the point-like scatterers is cube-shaped due to the characteristics of the k-Wave software when calculating the wave field. For the reconstruction of a single point-like scatterer, the locations of the scatterers are chosen as

$$D_1 = [-0.05, 0.05] \times [-0.05, 0.05] \times [-0.05, 0.05],$$

 $D_2 = [0.35, 0.45] \times [-0.85, -0.75] \times [0.15, 0.25].$

The location of a single point-like scatterer can be roughly identified even if the scatterer is not centered at the origin, the results can be seen in Fig. 10.

For the reconstructions of multiple point-like scatterers in \mathbb{R}^3 , the locations of the scatterers are chosen to be

$$D_3 = [0.55, 0.65] \times [0.75, 0.85] \times [0.95, 1.05],$$

 $D_4 = [-1.05, -0.95] \times [-0.85, -0.75] \times [-0.65, -0.55],$

respectively. The reconstructions can be seen in Fig. 11.

Example 4.7 (Reconstructions of cube scatterers). Consider the reconstructions of cube scatterers are considered in this example by choosing N=50, T=25 and $N_t=256$. Again, the forward scattering problem is solved utilizing the k-Wave software. The measurement points, the source points, the sampling grids and other parameters are the same as in Example 4.6. See Figs. 12 and 13 for the reconstructions. In Fig. 12, the cube is chosen as

$$D_5 = [-0.4, 0.8] \times [-0.4, 0.8] \times [-0.4, 0.8].$$

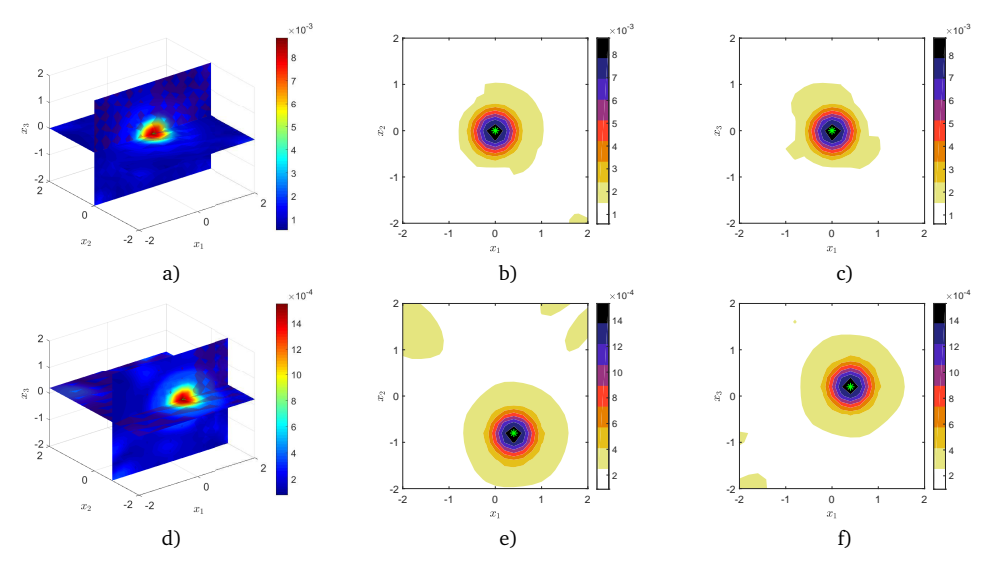


Figure 10: Reconstructions of a single point-like scatterer using the indicator function I_3 , $\varepsilon=5\%$. (a,d) The reconstructions of the scatterers D_1 and D_2 , respectively. (b,e) The slices through the center of the scatterers along the x_1 - x_2 plane. (c,f) The slices through the center of the scatterers along the x_1 - x_2 plane.

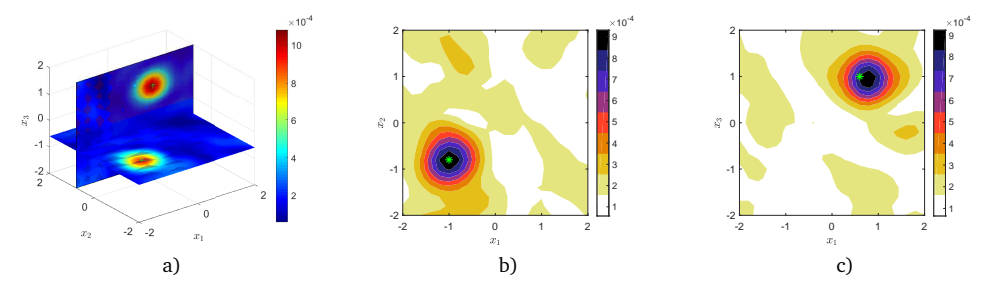


Figure 11: Simultaneous reconstruction of two point-like scatterers D_3 and D_4 using the indicator function I_3 , $\varepsilon=5\%$. a) The reconstruction of the scatterers. b) The slice through the center of the scatterer along the x_1 - x_2 plane. c) The slice through the center of the scatterer along the x_1 - x_2 plane.

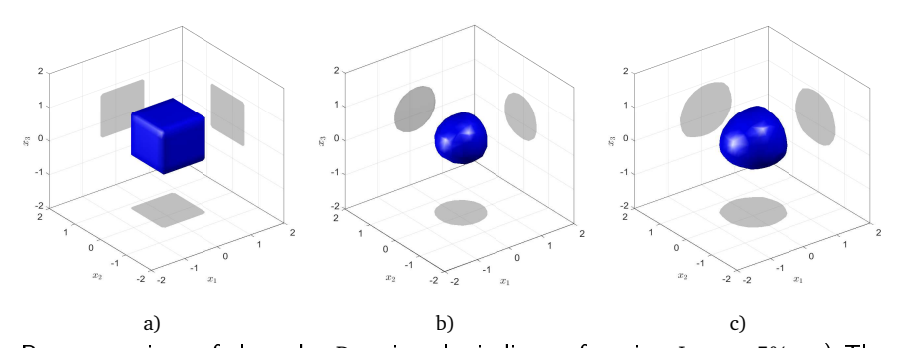


Figure 12: Reconstructions of the cube D_5 using the indicator function I_3 , $\varepsilon=5\%$. a) The geometry setting. b) The reconstruction of the cube with iso-surface level 0.02. c) The reconstruction of the cube with iso-surface level 0.015.

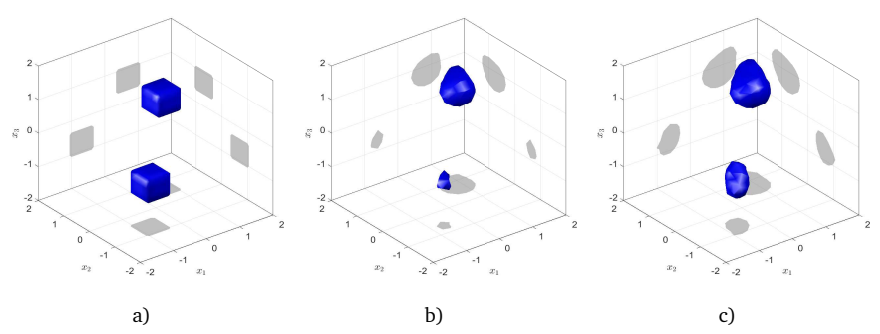


Figure 13: Simultaneous reconstructions of two disconnected cubes D_6 and D_7 using the indicator function I_3 , $\varepsilon=5\%$. a) The geometry setting. b) The reconstruction of the cubes with iso-surface level 0.008. c) The reconstruction of the cubes with iso-surface level 0.007.

In Fig. 13, the two disconnected cubes are chosen as

$$D_6 = [0.4, 1] \times [0.4, 1] \times [0.4, 1],$$

 $D_7 = [-1, -0.4] \times [-1, -0.4] \times [-1, -0.4],$

respectively. The noise level is chosen as $\varepsilon = 5\%$. This example shows that the algorithm based on the indicator function $I_3(z)$ could give the approximate positions of the cubes, but is no effective to determine the shape of the cubes.

5. Conclusion

Simple direct sampling methods based on the time convolution of the Green's function and the signal function have been provided to reconstruct point-like and normal size scatterers in this paper. Numerical examples in two and three dimensional spaces demonstrate the effectiveness and robustness of the methods.

Acknowledgments

The work of B.C. was supported by the National Natural Science Foundation of China (Grant No. 12101603) and by the Fundamental Research Funds for the Central Universities (the Special Project for Civil Aviation University of China (Grant No. 3122021072) and by the supplementary Project of Civil Aviation University of China (Grant No. 3122022PT19)).

References

- [1] L. Banjai and S. Sauter, *Rapid solution of the wave equation in unbounded domains*, SIAM J. Numer. Anal. **47**(1), 227–249 (2008).
- [2] G. Bao, S. Hou and P. Li, *Inverse scattering by a continuation method with initial guesses from a direct imaging algorithm*, J. Comput. Phys. **227**(1), 755–762 (2007).

- [3] G. Bao and J. Lin, *Imaging of local surface displacement on an infinite ground plane: The multiple frequency case*, SIAM J. Appl. Math. **71**, 1733–1752 (2011).
- [4] G. Bao and L. Zhang, *The acoustic scattering of a layered elastic shell medium*, Ann. Appl. Math. **39**, 462–492 (2023).
- [5] Y. Chang and Y. Guo, *Simultaneous recovery of an obstacle and its excitation sources from near-field scattering data*, Electron. Res. Arch. **30**(4), 1296–1321 (2022).
- [6] B. Chen, Y. Guo, F. Ma and Y. Sun, Numerical schemes to reconstruct three-dimensional time-dependent point sources of acoustic waves, Inverse Probl. **36**(7), 075009 (2020).
- [7] B. Chen, F. Ma and Y. Guo, *Time domain scattering and inverse scattering problems in a locally perturbed half-plane*, Appl. Anal. **96**(8),1303–1325 (2017).
- [8] B. Chen and Y. Sun, *A simple method of reconstructing a point-like scatterer according to time-dependent acoustic wave propagation*, Inverse Probl. Sci. En. **29**(12), 1895–1911 (2021).
- [9] Q. Chen, H. Haddar, A. Lechleiter and P. Monk, *A sampling method for inverse scattering in the time domain*, Inverse Probl. **26**(8), 085001 (2010).
- [10] Z. Chen and G. Huang, *Phaseless imaging by reverse time migration: Acoustic waves*, Numer. Math. Theory Methods Appl. **10**(1), 1–21 (2017).
- [11] D. Colton and A. Kirsch, *A simple method for solving inverse scattering problems in the resonance region*, Inverse Probl. **12**(4), 383 (1996).
- [12] D. Colton and R. Kress, *Inverse Acoustic and Electromagnetic Scattering Theory*, Springer (2013).
- [13] H. Dong, W. Ying and J. Zhang, *An efficient Cartesian grid-based method for scattering problems with inhomogeneous media*, Numer. Math. Theor. Meth. Appl. **16**, 541–564 (2023).
- [14] Y. Guo, D. Hömberg, G. Hu, J. Li and H. Liu, *A time domain sampling method for inverse acoustic scattering problems*, J. Comput. Phys. **314**, 647–660 (2016).
- [15] Y. Guo, P. Monk and D. Colton, *Toward a time domain approach to the linear sampling method*, Inverse Probl. **29**(9), 095016 (2013).
- [16] H. Haddar, A. Lechleiter and S. Marmorat, *An improved time domain linear sampling method for Robin and Neumann obstacles*, Appl. Anal. **93**(2), 369–390 (2014).
- [17] J. Lai, M. Li, P. Li and W. Li, A fast direct imaging method for the inverse obstacle scattering problem with nonlinear point scatterers, Inverse Probl. Imaging. **12**(3), 635–665 (2018).
- [18] K.H. Leem, J. Liu and G. Pelekanos, Two direct factorization methods for inverse scattering problems, Inverse Probl. **34**(12), 125004 (2018).
- [19] J. Li, H. Liu, H. Sun and J. Zou, *Imaging acoustic obstacles by singular and hypersingular point sources*, Inverse Probl. Imaging. 7(2), 545–563 (2013).
- [20] J. Li, H. Liu and Q. Wang. Enhanced multilevel linear sampling methods for inverse scattering problems, J. Comput. Phys. 257, 554–571 (2014).
- [21] J. Li, H. Liu and J. Zou, *Multilevel linear sampling method for inverse scattering problems*, SIAM J. Sci. Comput. **30**(3), 1228–1250 (2008).
- [22] J. Li, H. Liu and J. Zou, *Strengthened linear sampling method with a reference ball*, SIAM J. Sci. Comput. **31**(6), 4013–4040 (2009).
- [23] H. Liu and X. Liu, *Recovery of an embedded obstacle and its surrounding medium from formally determined scattering data*, Inverse Probl. **33**(6), 065001 (2017).
- [24] X. Liu, A novel sampling method for multiple multiscale targets from scattering amplitudes at a fixed frequency, Inverse Probl. 33(8), 085011 (2017).
- [25] F.J. Sayas, Retarded Potentials and Time Domain Boundary Integral Equations: A Road Map, Springer (2016).
- [26] Y. Sun, Indirect boundary integral equation method for the Cauchy problem of the Laplace equation, J. Sci. Comput. **71**(2), 469–498 (2017).

- [27] Y. Sun, X. Lu and B. Chen, *The method of fundamental solutions for the high frequency acoustic- elastic problem and its relationship to a pure acoustic problem*, Eng. Anal. Bound. Elem. **156**(11), 299–310 (2023).
- [28] B.E. Treeby and B.T. Cox, *K-wave: Matlab toolbox for the simulation and reconstruction of photoacoustic wave-fields*, J. Biomed. Opt. **15**, 021314 (2010).
- [29] Y. Yue, F. Ma and B. Chen, *Time domain linear sampling method for inverse scattering problems with cracks*, East Asian J. Appl. Math. **12**(1), 96–110 (2022).
- [30] D. Zhang, Y. Guo, Y. Wang and Y. Chang, *Co-inversion of a scattering cavity and its internal sources: Uniqueness, decoupling and imaging*, Inverse Probl. **39**(6), 065004 (2023).
- [31] M. Zhao, J. He and L. Wang, *Numerical solutions of the electromagnetic scattering by overfilled cavities with inhomogeneous anisotropic media*, Commun. Comput. Phys. **34**, 530–562 (2023).